

1 **Determination of persistence effects in spatio-temporal patterns of**
2 **upward long-wave radiation flux density from an urban**
3 **courtyard by means of time-sequential thermography**

4

5 Fred Meier, Dieter Scherer, Jochen Richters

6 Technische Universität Berlin, Department of Ecology, Chair of Climatology,

7 Rothenburgstraße 12, D-12165 Berlin, Germany

8

9 Abstract

10 This research analyses upward long-wave radiation flux density from urban surfaces using a
11 high-resolution thermal-infrared (TIR) camera and meteorological measurements in the city
12 of Berlin, Germany. We report spatio-temporal patterns of the difference between upward
13 long-wave radiation flux density from courtyard surfaces and the roof. For temporal analysis,
14 the TIR camera recorded one TIR image per minute over a period of two days from 3rd to 5th
15 May 2007. Three-hourly averaged thermal patterns show persistence effects due to shadow,
16 sky view factor (SVF) distribution in the courtyard, thermal properties of the surface
17 materials, human activities and turbulence characteristics of the surface-atmosphere interface.
18 The history of shadow influences the 24-hourly mean pattern. Shadow caused by temporarily
19 parked cars results in a lower upward long-wave radiation flux density compared to the non-
20 shadowed surface close to it. Immediately after car departure, this difference decreases. We
21 propose a method to derive the thermal admittance of a concrete surface based on TIR data
22 from this attenuation process. This study shows that ground-based high-resolution TIR
23 imagery is highly suitable to investigate surface thermal properties and dynamic processes
24 controlling thermal patterns within a complex three-dimensional (3D) urban structure.

25 1. Introduction

26 The urban surface reveals a complex three-dimensional (3D) structure creating strong micro-
27 scale variations of upward long-wave radiation. These spatio-temporal patterns have several
28 reasons e.g. different radiative and thermal properties of the individual urban surfaces,
29 different radiation regimes depending on slope and aspect of the facets, including adjacency
30 effects, multiple reflections, different sky-view factors (SVF) and shadows caused by objects
31 in the immediate neighbourhood (Sugawara & Takamura 2006, Voogt & Oke 2003,
32 Kobayashi & Takamura 1994, Oke 1987). Radiation in the thermal-infrared (TIR) part of the
33 electromagnetic spectrum is an essential variable both in the radiation budget and the energy
34 balance of the Earth's surface. Surface temperature directly controls emission of long-wave
35 radiation but is also the result of energy exchange between atmosphere and bordering
36 surfaces. Tower measurements using pyranometers and pyrgeometers have shown the large
37 contribution of upward long-wave radiation to the surface radiation budget (e.g. Christen &
38 Vogt 2004).

39

40 *1.1 Time-Sequential Thermography (TST)*

41 The unavoidable trade-off between spatial and temporal resolution inherent to satellite-based
42 remote sensing, and the relatively high costs of flight campaigns generate a significant
43 problem for acquisition of spatially distributed TIR data at both high spatial and high
44 temporal resolution. Higher spatial resolution data can be used to study changes in thermal
45 patterns between daytime and nighttime at surface material level (Quattrochi & Ridd 1994, Lo
46 et al. 1997). The diurnal course of urban surface temperatures can be obtained by flight
47 campaigns (Lagourde et al. 2004, Voogt & Oke 1998). The combination of several satellite
48 sensors, e.g. MODIS, NOAA-AVHRR and Landsat-ETM is suitable to derive the diurnal
49 course of upward long-wave radiation and can achieve good results in comparison with in-situ

50 pyrgeometer measurements (Rigo et al. 2006). Ground-based remote sensing using TIR
51 camera systems mounted on masts, towers or building roofs provide an alternative to airborne
52 and satellite platforms. Voogt & Oke (2003) expect progress in urban climate research due to
53 availability and application of low-cost, high-resolution portable TIR scanner systems. In
54 Tokyo, a TIR camera system continuously measured urban surface temperatures for
55 derivation of a town-scale thermal property parameter (Sugawara et al. 2001). At the building
56 scale, Hoyano et al. (1999) used time-sequential thermography (TST) for calculating sensible
57 heat flux density. Thermal characteristics of various urban surfaces in Tel-Aviv were assessed
58 using TST over a diurnal period at high spatial resolution by using a thermal video radiometer
59 that captured images from a fixed position in a specific time interval (Chudnovsky et al.
60 2004).

61

62 *1.2 Objectives*

63 The general objective of this paper is to assess micro-scale urban surface thermal patterns
64 concerning the persistence of thermal patterns inside an urban courtyard. In detail, we address
65 the following two questions:

66

67 1.) How important is the history of shadow for upward long-wave radiation flux density from
68 courtyard surfaces in relation to the diurnal cycle?

69 2.) Can we observe different persistence effects in spatio-temporal patterns of upward long-
70 wave radiation flux density during daytime and nighttime hours?

71

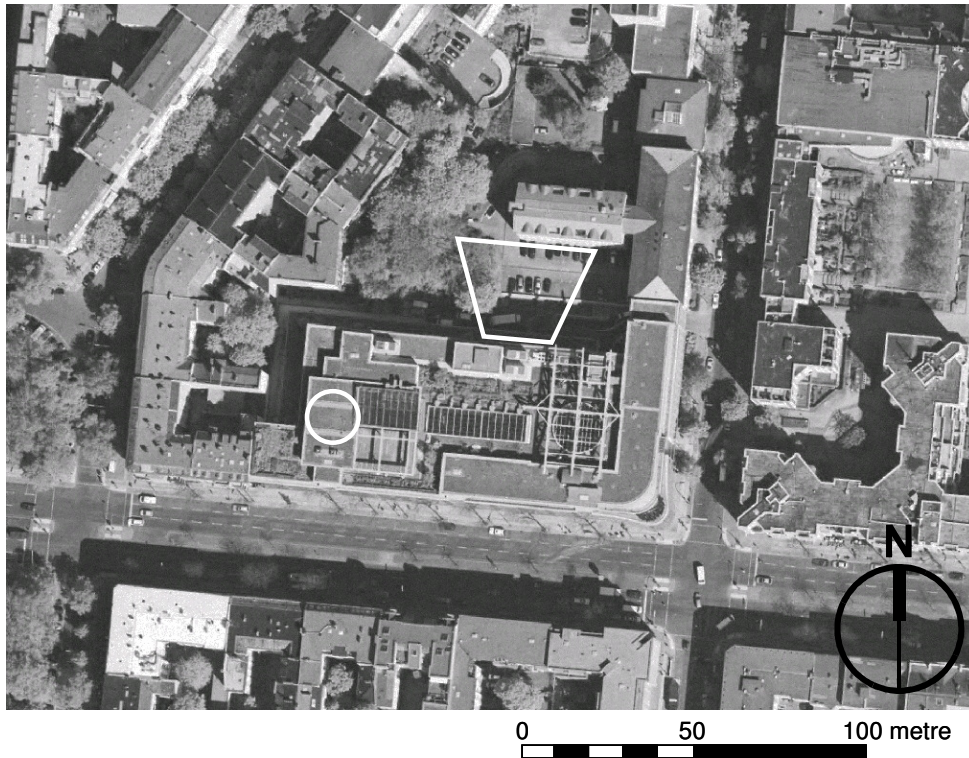
72 Considering the assumption that thermal persistence effects depend on thermal properties of
73 surfaces, we also discuss an approach to determine the thermal admittance of a concrete
74 surface. For these purposes, we observe and analyse spatio-temporal variability of upward

75 long-wave radiation flux density using an oblique viewing high-resolution TIR camera system
76 capturing images at scales in the range of centimetres. We expect some variability in surface
77 temperature due to emissivity differences at this micro-scale. Measurements of emissivity for
78 all surfaces in the field of view (FOV) are beyond the scope of this project. Therefore, this
79 paper focuses on upward long-wave radiation. A further remaining problem of thermal remote
80 sensing deals with directional variations of measured long-wave radiation, referred to as
81 thermal anisotropy (e.g. Voogt 2008). This aspect is not included in this paper.

82

83 *1.3 Persistence phenomena in urban areas*

84 The 3D city structure generates a complex pattern of partially sunlit and shadowed surfaces in
85 particular under cloudless conditions. In a northern hemisphere square courtyard, the shadow
86 always moves from West to East. In Fig. 1, the investigated courtyard is divided into a sunlit
87 and a shadowed area, visible by sharp borders. The small treeless courtyards to the West are
88 completely shadowed. Depending on shadow, different surfaces receive different short-wave
89 irradiance. In a more general perspective, a thermal persistence effect is activated by a
90 specific disturbance in the surface-atmosphere system. A question is how long is this
91 disturbance detectable in the system? In urban areas, the disturbance is to be manifested in the
92 3D city structure or due to human activities like shadow for instance due to parked cars. The
93 high-spatial resolution infrared image simulator OSIRIS reproduces the persistence of shadow
94 effects in complex urban environments (Pogliano et al. 2006). Within high-rise buildings,
95 extensive shadow can produce sufficient surface cooling to induce an inversion of near-
96 surface air temperature (Ruffieux et al. 1990). Other urban climate phenomena like the
97 daytime cool island resulting partly from shadow effects (e.g. Nichol 2006, Erell &
98 Williamson 2006). Impacts of shadow effects are also included in numerical simulations of
99 interactions between the 3D urban surface and the atmosphere (e.g. Bruse & Fler 1998).



100
101
102
103
104
105

Fig. 1: Aerial photo of the study site and surrounding area in Berlin, district Charlottenburg-Wilmersdorf, with FOV of the TIR camera inside the investigated courtyard and FOV of the down-facing pyrgeometer (Kipp & Zonen, CNR1) on the Stilwerk building roof (aerial photo with permission of Berlin Department of Urban Development, Urban and Environmental Information System).

106 **2. Methods**

107 This section specifies the study site and the experimental setup, pre-processing steps of the
108 TIR imagery and the basic idea and equations for determination of persistence effects.

109

110 *2.1 Study site and experimental setup*

111 The study site is located in Berlin (Germany) in the Charlottenburg-Wilmersdorf district close
112 to the city centre Zoologischer Garten (City-West). City structure is characterized by five to
113 six-story perimeter block development (see also Fig. 1). Previous investigations in Berlin
114 concentrated on the relationship between land use data and surface temperature derived from
115 Landsat data (Munier & Burger 2001) or from airborne remote sensing (Kottmeier et al.
116 2007). Endlicher & Lanfer (2003) articulate another interesting inter-relation between the
117 thermal behaviour of urban surfaces and their influence on environmental conditions for

118 plants and animals at the micro-scale. They pointed out that the urban heat island and
 119 heterogeneity in long-wave radiation regimes in cities leads to new biodiversity patterns
 120 particular due to intrusion of non-native plants. Courtyards as a typical open space in Berlin
 121 were investigated with regard to spatial variations of thermal comfort, which depends on size
 122 and vertical building structure (Mertens 1999).

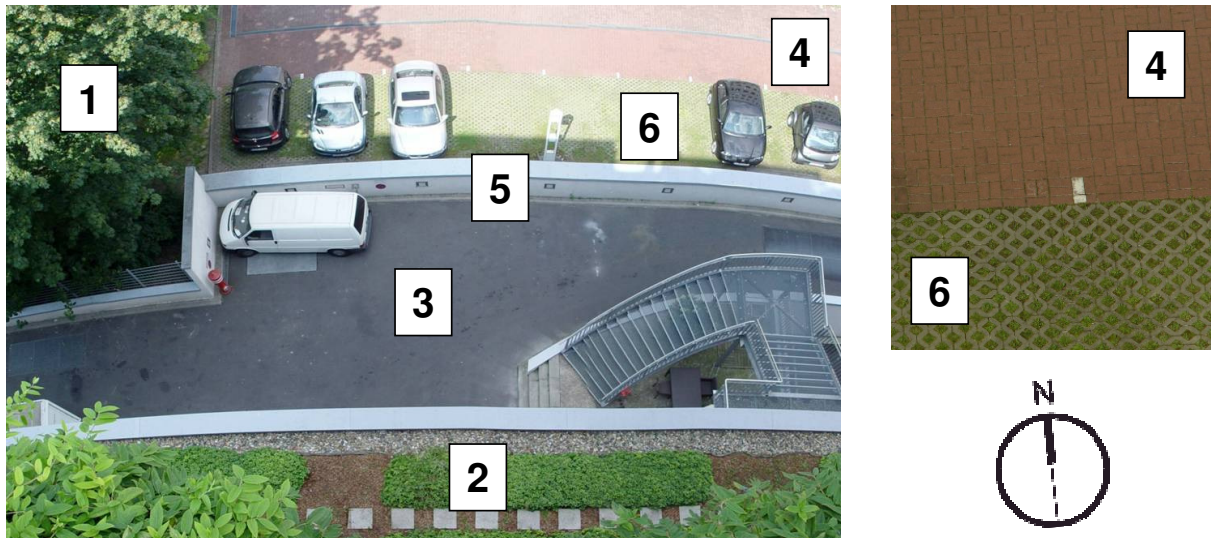
123 This micro-scale TIR remote sensing study was part of a local-scale urban climatology
 124 experiment including boundary layer meteorological measurements such as directly measured
 125 sensible heat flux density, air temperature and humidity. We call it ‘Stilwerk Experiment’
 126 according to the name of the shopping mall, whose roof provided a basis for measurement
 127 installations. Intensive experimental work was conducted between 20th April and 14th May
 128 2007. Technical specifications of the TIR camera system are summarised in Table 1.

129 **Table 1: Technical specifications of the thermal-infrared (TIR) camera**

Camera manufacturer	InfraTec
Camera model	VarioCam® head
Spectral range	7.5 µm – 14 µm
Detector type	Microbolometer Focal Plane Array (320 x 240 pixel), uncooled
Temperature resolution at 30°C	better than 0.1 K
Measurement accuracy	± 2 K, ± 2%
Lens	Standard wide angle lens 12.5 mm
Field of View (FOV)	64° x 50°

130

131 For spatial analysis, we selected an oblique viewing position from the roof. The TIR camera
 132 was oriented towards North (354°) and inclined by 20° from the nadir angle. In the courtyard
 133 FOV the essential features (see numbering in Fig. 2) are one lime tree (1), a narrow green
 134 terrace (2), situated 9.4 m above street level, an asphalt loading zone (3) belonging to the
 135 department store and a car-park (4) belonging to the opposite building, separated by a small
 136 wall (5). The terrace consists of two small hedgerows, paving tiles and gravel. Concrete
 137 paving stones (4) and honeycomb-type paving stones with grass (6) cover the car-park area.



138
 139 **Fig. 2: Photograph showing approximately the FOV of the TIR camera (photograph courtesy of J. Rogée,**
 140 **Technische Universität Berlin). Description of the numbered features in the courtyard: lime tree (1),**
 141 **terrace with hedgerow, gravel and paving tiles (2), asphalt loading zone (3), concrete paving stones (4),**
 142 **wall (5) and honeycomb-type paving stones with grass (6).**

143

144 The geometric resolution of a pixel closer to the lens is higher than in the background due to
 145 of the oblique view. The geometric resolution changes from approx. 3.6 cm to 10.8 cm
 146 depending on distance between sensor and target. Here distance varies between approx. 10 m
 147 for the terrace pixels and approx. 30 m for the farthest car-park pixels. The TIR camera
 148 recorded one image per minute over a period of 48 hours from 3rd to 5th May 2007. The fixed
 149 position ensures a valid comparison between the multi-temporal imagery on the same spatial
 150 basis and an accurate geometric co-registration respectively. All four components of the
 151 radiation balance were measured two metres above the building roof. Measurement frequency
 152 of the device (Kipp & Zonen, CNR1) was 1 Hz and we used a 1 min averaging interval.

153 Upward long-wave radiation from the roof FOV represents a mixed signal of components of
 154 the extensive green roof structure i.e. sedum, herbs, grass and a couple of concrete paving
 155 tiles (30 cm x 30 cm). During the TST operation period the substrate of the extensive green
 156 roof was very dry because of very low precipitation in April and the first half of May 2007.

157

158 *2.2 Pre-processing, radiometric and geometric corrections steps of TIR imagery*

159 The TIR camera system provides calibration metadata for each recorded image, derived from
160 firmware calibration using laboratory blackbody temperatures. Depending on case
161 temperature, the system generates calibration metadata in a user-defined frequency. The first
162 step of image processing uses these internal calibration parameters for converting measured
163 radiance into directional brightness temperatures (T_b) for each pixel. This assumes that the
164 detected surface is a Lambertian blackbody. In order to avoid drift effects the internal image
165 calibration file has to be updated in the same interval, or at higher frequency, than the
166 measurement interval. If the system operates with an internal calibration frequency lower than
167 the measurement interval then minor artificial jumps from one image acquisition to the next
168 are possible resulting from unconsidered changes in case temperature.

169 Lens effects disturb TIR data. Experiments showed a clear 1.2 K difference of T_b from the
170 centre of the TIR image to the corners. This lens effect was corrected by using a data set of
171 dense fog and assuming isotropic distribution of radiance (Christen et al. 2006). Other
172 experiments with TIR cameras using wide-angle lenses (Lagouarde et al. 2000, 2004) also
173 reported such effects. They relate this problem to vignetting effects leading to reduced
174 brightness in the periphery compared to the central part.

175 Lenses generally produce intrinsic geometric distortions. In our laboratory, these
176 deformations have been analysed by measuring a grid of metallic pins in a regular square
177 pattern. We used the positions of the metallic pins to construct a Delaunay triangulation of a
178 planar set of points. Then the geometrical deviations in x- and y-direction were interpolated
179 for each image pixel. By using a nearest-neighbour technique, the TIR image pixels can be
180 shifted to their real positions. After correction for lens deformation, the TIR image covers a
181 FOV of 57.5° by 44.7° .

182 We worked without an atmospheric correction procedure, due to short target-sensor distances
183 in our experimental setup and therefore short atmospheric path lengths. Between adjacent

184 surfaces, radiance differences caused by atmospheric effects are generally smaller than
185 measurement errors. Finally, T_b was reconverted into long-wave radiation flux density via
186 Stefan-Boltzmann law:

$$187 \quad \hat{E}_{TST}(\bar{x}_i, t) = \sigma T_b^4(\bar{x}_i, t), \quad (1)$$

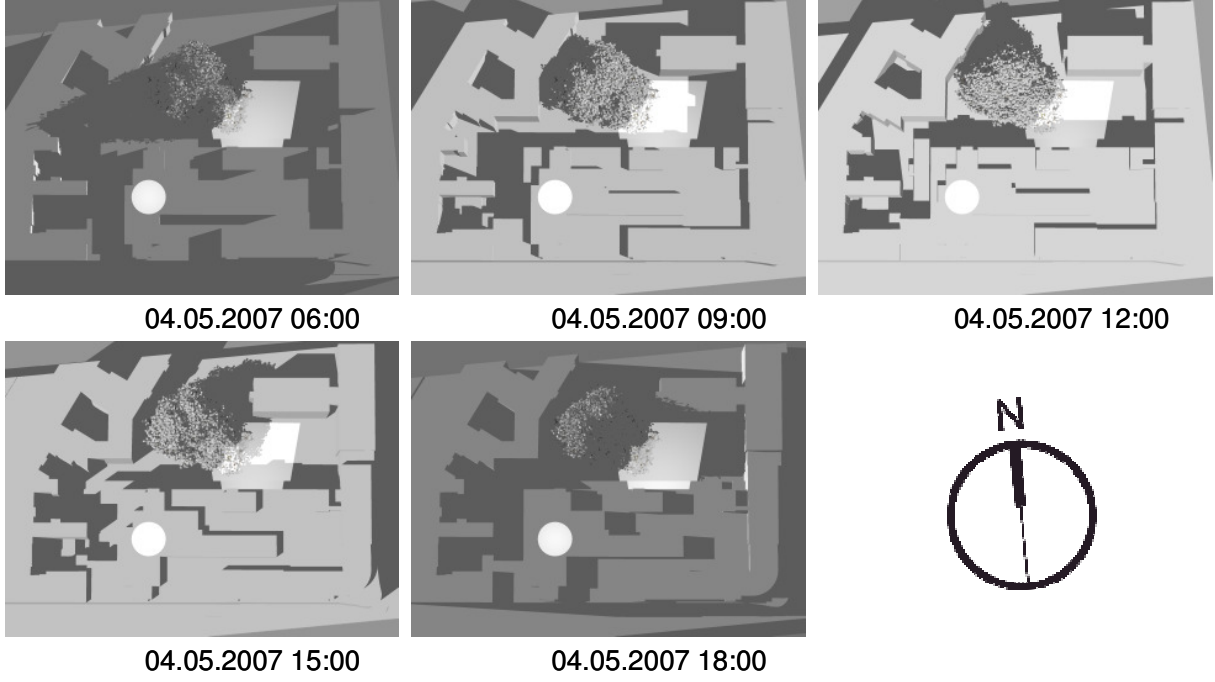
188 where \bar{x}_i represents each pixel and its spatial position in the courtyard, t is the acquisition
189 time of the TIR image and σ is Stefan Boltzmann's constant. The resultant imagery

190 $\hat{E}_{TST}(\bar{x}_i, t)$ consists of 2880 TIR images that can be considered as a spatio-temporal image-
191 cube.

192

193 *2.3 Determination of persistence effects*

194 Persistence in this paper means a temporal stability of spatial patterns of upward long-wave
195 radiation flux density. The basic idea in order to determine persistence effects is to compare a
196 temporarily disturbed surface with an undisturbed reference surface. We defined shadow as
197 the disturbance. Simply because the building roof is always non-shadowed and in order to
198 determine persistence effects in relation to the diurnal cycle, we selected the roof as a
199 reference surface. The scenes in Fig. 3 show the shadow in the study area in three-hourly
200 intervals during daytime at 4th May 2007. The highlighted area in the courtyard shows the
201 FOV of the TIR camera during the TST investigation period. The highlighted circular area
202 represents the 150° FOV of the down-facing pyrgeometer. The FOV of the TIR camera
203 covers a complex shadow situation due to building walls and tree crown. The FOV on the
204 roof is always non-shadowed.



205

206 **Fig. 3: Visualisation of shadow in the radiative source areas for roof (circle) and courtyard (trapeze)**
 207 **measurements at 06:00, 09:00, 12:00, 15:00 and 18:00 on 4th May. Time specification refers to Central**
 208 **European Time (CET).**

209

210 Thus, we computed the difference between upward long-wave radiation from every courtyard
 211 pixel and long-wave radiation $\hat{E}_{LW_ROOF}(t)$ from the roof.

$$212 \quad \uparrow \Delta E(\bar{x}_i, t) = \uparrow E_{TST}(\bar{x}_i, t) - \uparrow E_{LW_ROOF}(t) \quad (2)$$

213 Then we defined temporal stability for final persistence determination by computing a
 214 temporal average. The spatio-temporal patterns of mean difference (*MD*) as well as the
 215 standard deviation of difference (*SDD*) and mean rate of change of difference (*MROCD*)
 216 provide the basis for persistence analysis.

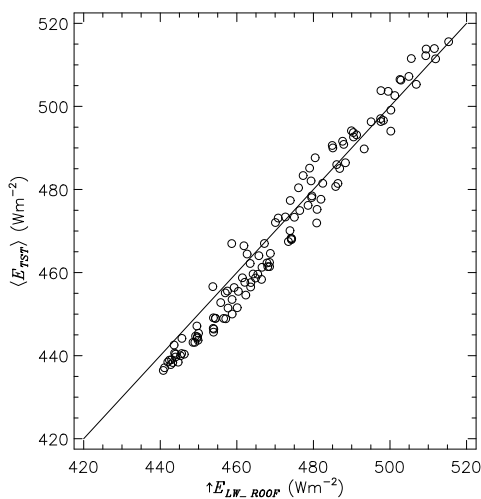
$$217 \quad MD = \overline{\uparrow \Delta E(\bar{x}_i, t)} \quad (3)$$

$$218 \quad SDD = \sigma(\uparrow \Delta E(x_i, t)) \quad (4)$$

$$219 \quad MROCD = \overline{\frac{\delta}{\delta t}(\uparrow \Delta E(\bar{x}_i, t))} \quad (5)$$

220 The *MD* pattern indicates the presence of a persistence effects, the *SDD* pattern comprises
 221 information about the intensity of a disturbance in relation to the undisturbed reference

222 surface and the *MROCD* pattern shows if the disturbance produced a positive or negative
 223 change in upward long-wave radiation from courtyard surfaces. The overbar in Eq. 3 and 5
 224 denotes the temporal average. A more detailed discussion concerning the temporal variability
 225 of selected areas of interests (AOI) follows in the discussion section.
 226 There are some assumptions underlying this approach. First, we disregard the spectral range
 227 discrepancy. The CNR1 pyrgeometer is a broadband (3 μm to 100 μm) and the TIR camera is
 228 a narrowband measurement device. During the Stilwerk Experiment on 30th April from 13:30
 229 to 15:30, the TIR camera system was installed on the roof for comparison between $\uparrow E_{LW_ROOF}$
 230 and the spatial mean of the TIR image $\langle E_{TST} \rangle$ by matching both FOV approximately. Both
 231 datasets are strongly correlated ($r^2 = 0.97$) and the root mean square error (RMSE) is 4.7
 232 W m^{-2} , which is less than the CNR1 pyrgeometer measurement accuracy (see Fig. 4).
 233 Secondly, we have to consider that measured upward long-wave radiation include reflections
 234 from downward long-wave radiation because surface emissivity values are less than unity.
 235 Nevertheless, the interpretation of upward long-wave radiation from low emissivity surfaces
 236 is critical in this respect e.g. from all metallic mainly car surfaces in the courtyard.



237
 238 **Fig. 4: Comparison between upward long-wave radiation flux densities from the roof measured by down-**
 239 **facing pyrgeometer and TIR camera.**

240

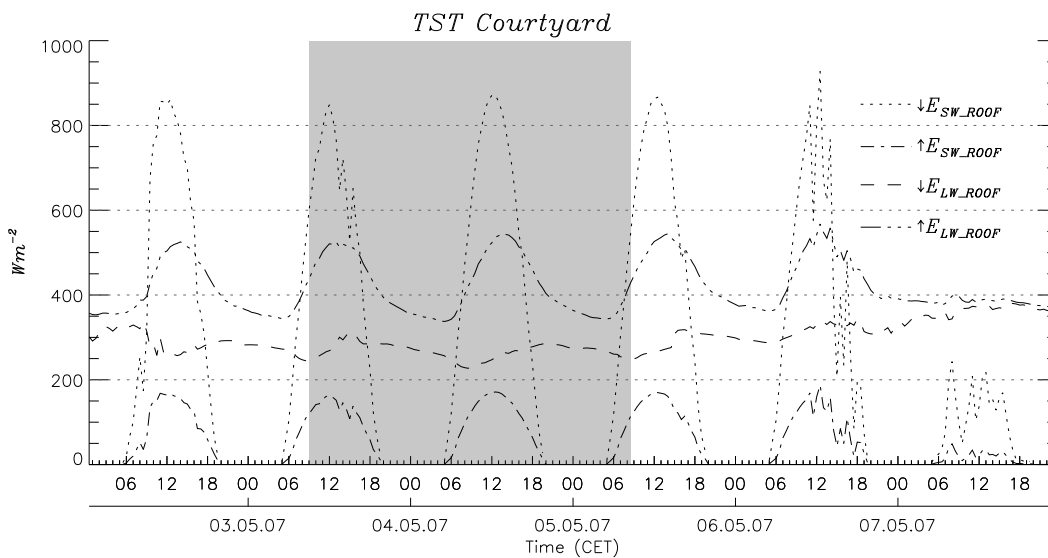
241 3. Results

242 In the results, we present spatio-temporal patterns of *MD*, *SDD* and *MROCD* for a three-
243 hourly and a 24-hourly temporal average using a percentile visualization approach. At first,
244 we show all radiation balance components from the CNR1 measurement device.

245

246 3.1 Radiation balance components

247 During the investigation period, clear sky conditions caused high downward short-wave
248 irradiance ($\downarrow E_{SW_ROOF}$) with a maximum of 870 W m^{-2} around noon. Particularly on 4th May
249 all four radiation components have a characteristic diurnal cycle curve (see Fig. 5). These
250 atmospheric conditions allow for detailed analysis of the diurnal variation in upward long-
251 wave radiation.



252

253 **Fig. 5: All four radiation components from the CNR1 measurement device 2 m above the Stilwerk**
254 **building roof (30 min average) and courtyard TST investigation period (grey box).**

255

256 3.2 Spatio-temporal patterns – percentile visualization approach

257 Contrast within an image is based on brightness or darkness of a pixel in relation to other

258 pixels. Modifying the contrast can enhance the ability to extract pattern information from the

259 image. A simple way to modify contrast is to scale the pixel values within an image. Hence,
 260 we scaled the pixel values of all mean patterns (*MD*, *SDD* and *MROCD*) between the 95%
 261 percentile (maximum brightness) and the 5% percentile (minimum brightness) of the original
 262 computed mean patterns. This linear grey-scaling approach for visualization does not allow a
 263 direct comparison between the single three-hourly patterns. Furthermore, all grey-scale bars
 264 have benchmarks for the median (50%), the minimum, maximum and zero value of the
 265 computed mean pattern.

266

267 3.3 Thermal patterns of three-hourly periods

268 For a more detailed analysis of the different thermal regimes during day and night we present
 269 temporal mean patterns of three-hourly periods. For instance, the *MD* pattern was calculated
 270 as follows:

$$271 \quad MD = \frac{1}{180} \sum_{i=1}^{180} \uparrow \Delta E(\bar{x}_i, t). \quad (6)$$

272 Therefore, Fig. 6 consists of 24 patterns arranged in eight rows (A-H) which represent the
 273 temporal mean patterns of all three-hourly periods from 06:01 to 06:00 next morning. Row A
 274 shows the patterns for *MD* (left), *SDD* (middle) and *MROCD* (right) from 06:01 to 09:00 on
 275 4th May 2007. All *MROCD* patterns illustrate the mean rate of change for $\delta t = 1 \text{ min}$ (Eq. 5).
 276

277 3.3.1 MD patterns of three-hourly periods

278 During the day, the median of the *MD* patterns is negative. The lowest three-hourly median is
 279 -123.4 W m^{-2} and belongs to the early afternoon period from 12:01 to 15:00 (Fig. 6c, left).
 280 Still after sunset the median remains negative (Fig. 6e, left). There are some areas with
 281 positive *MD* values during daytime. In the morning hours, a thermal hot spot corresponds to
 282 sunlit surfaces in the northwestern part of the courtyard in particular to the metallic car
 283 surfaces. In shadowed areas, only the hot automotive engines (Fig. 6a, left, white box) have

284 positive *MD* values. The treetop shows a heterogeneous pattern due to the existence of both
285 sunlit and shadowed treetop areas.

286 At night, all used parking spaces show lower *MD* values in contrast to the space between
287 them. This pattern shows the influence of parked cars on the underlying surface in terms of
288 thermal radiation. From 21:01 to 24:00, the treetop has slight positive *MD* values between 5
289 W m^{-2} and 24 W m^{-2} . This range probably depends on the SVF of the individual leaves and
290 the air temperature inside the treetop. The lowest *MD* values correspond to higher situated
291 leaves at the crown apex. This *MD* pattern can be associated with the theoretical treetop SVF
292 distribution and is comparable to the results of the urban-park scale model experiment carried
293 out by Spronken-Smith & Oke (1999). The patches of higher *MD* values might also indicate
294 the influence of a higher air temperature inside the canopy. In general, air temperature is
295 important in setting leaf temperature and therefore emission of long-wave radiation (Oke
296 1987, p. 121). At night, (Fig. 6f, left) the eastern car-park area covered by concrete pavement
297 has the highest *MD* values between 50 W m^{-2} and 55 W m^{-2} . Only the building terrace has
298 negative *MD* values (Fig. 6f, left). At the end of the night, the median (see Fig. 6g and 6h,
299 left) increased marginally from 20.9 W m^{-2} to 22.1 W m^{-2} .

300

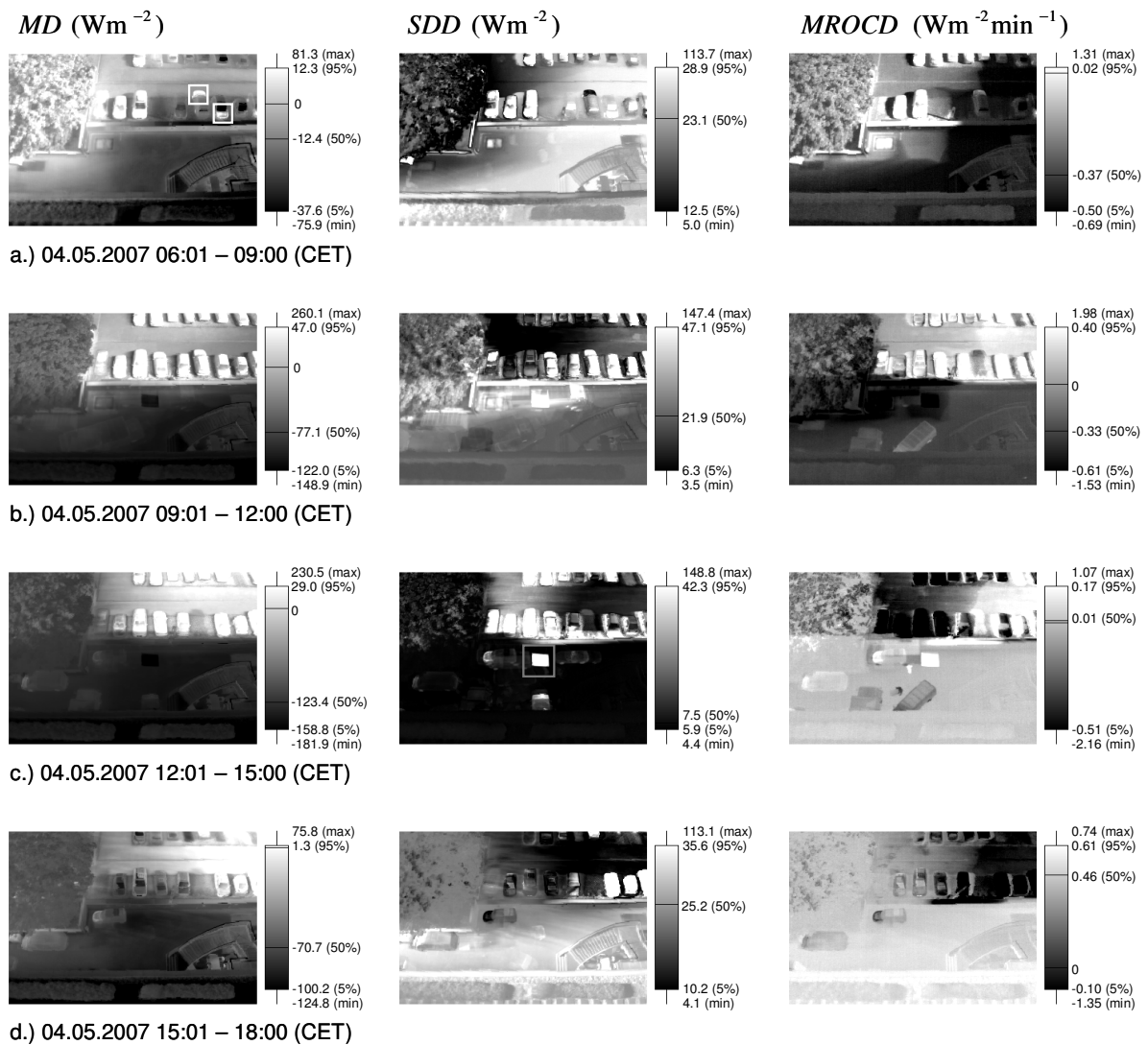
301 *3.3.2 SDD patterns of three-hourly periods*

302 High *SDD* values are the result of an alteration between direct-beam irradiance and diffuse
303 irradiance. In the noon period from 12:01 to 15:00 formerly sunlit areas like the car-park
304 drops into the tree shadow (Fig. 6c, middle). In the afternoon (Fig. 6d, middle) formerly
305 shadowed surfaces like the whole terrace and the loading zone receive now direct solar
306 irradiance. At the same time, the cars in the upper-right area drop into shadow, which caused
307 high *SDD* values. During low Sun elevations, the median of the *SDD* patterns is generally
308 higher, and amount to 23.1 W m^{-2} for the morning period and 25.2 W m^{-2} for the afternoon

309 period. The highest *SDD* values correspond to sunlit metallic car surfaces. Vehicle
310 movements also influence the *SDD* pattern. In Fig. 6c (middle, grey box) a quadratic shape
311 shows high *SDD* values corresponding to a metallic tailboard.

312 At night, all *SDD* values are generally lower in comparison to the day. The loading zone and
313 the small vertical wall exhibit the highest *SDD* values (Fig 6f, middle). Formerly used car-
314 park spaces show higher *SDD* than the non-used spaces. Surprisingly at the end of the night,
315 the car-park shows a contrary thermal pattern i.e. formerly used car-park spaces show lower
316 *SDD* values (Fig. 6h, middle). Parts of the terrace, the eastern part of the car-park and the
317 treetop have the lowest *SDD* values during the night. Some treetop branches draw attention
318 because of higher *SDD* values (Fig. 6f, middle).

319



320

321

Figure 6: Spatio-temporal patterns of mean difference (*MD*) (left column), standard deviation of difference (*SDD*) (middle column) and mean rate of change of difference (*MROCD*) (right column) between upward long-wave radiation from the courtyard and upward long-wave radiation from the roof for three-hourly periods.

322

323

324

325

326

3.3.3 *MROCD* patterns of three-hourly periods

327

In particular, *MROCD* pattern interpretation has to consider the relation between courtyard

328

and roof at the beginning of the analysed period. During the morning and noon periods

329

negative *MROCD* values mark an alteration resulting from lower heating rates for the

330

courtyard surfaces since the beginning of the three-hourly period. Positive *MROCD* values

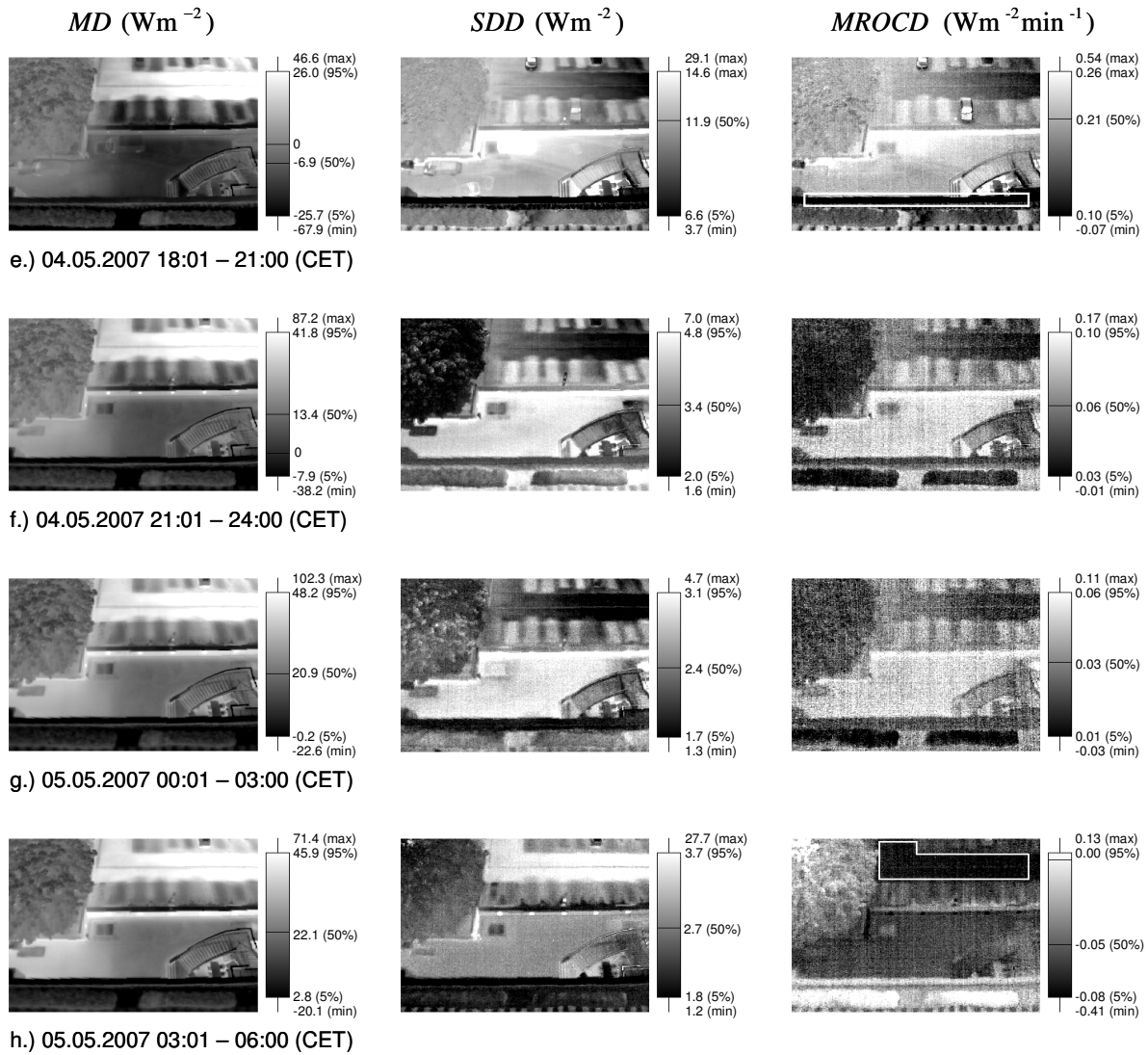
331

mark a period of higher heating rates for the courtyard surfaces. The opposite interpretation

332

applies to the cooling period of the roof surface from 14:00 to 05:30 next morning.

333 Relatively sharp borders are detectable in the *MROCD* daytime patterns. In Fig. 6a, (right)
334 one border marks the building shadow situation at the end of the period. Even roof eaves are
335 recognisable in this pattern. During the morning period, almost 50 % of the courtyard surfaces
336 show negative *MROCD* values and accordingly minor heating rates in comparison to the roof.
337 The migration of the building shadow across the loading zone and lower parts of the treetop
338 induces a pattern with negative *MROCD* values (Fig. 6b, right). In the afternoon the migration
339 of shadow across the car-park (Fig. 6c and 6d, right) becomes apparent. In particular, car
340 surfaces respond very strongly, if they drop into shadow. The narrow area showing the lowest
341 *SDD* and *MROCD* values (Fig. 6e, middle and right, white box) is the metallic cover-plate of
342 the terrace border. Later (Fig. 6f, right) the treetop and hedgerow are able to achieve nearly
343 similar cooling rates like the roof (*MROCD* values around zero). During 21:01 and 24:00
344 (Fig. 6f, right) the small wall in the courtyard has the highest *MROCD* values. The cooling
345 rate of this vertical surface is lower in comparison to the roof due to the low SVF.
346 The interpretation of nighttime *MROCD* patterns is a critical issue due to essentially very low
347 values. However, it is possible to identify different features in the courtyard. The whole car-
348 park area covered by concrete pavers is visible as a homogenous surface structure at the end
349 of the night (Fig. 6h, right, white box). This pattern implies a minor influence of SVF at the
350 end of the night, because this pattern refers more to the different surface materials than to the
351 different SVF in the courtyard. Furthermore, the *MROCD* patterns show attenuation
352 accompanied by a decrease of the *MROCD* median and a finally slight negative *MROCD*
353 median. The nighttime pattern from 03:01 to 06:00 is partly influenced by incident short-wave
354 radiation from sunrise resulting in higher values for tree crown apex, but this fact does not
355 explain the whole pattern of this three-hourly period. Hence, at the end of the night *MROCD*
356 values could be more influenced by other processes. In the discussion, we will try to explain
357 this result based on selected AOI and atmospheric variables.



358
359 **Figure 6: continued (three-hourly nighttime patterns).**

360

361 *3.4 Thermal patterns of a 24-hourly period*

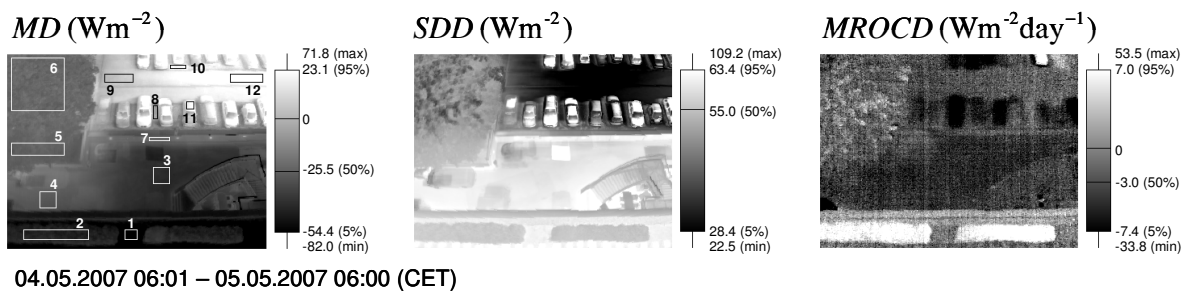
362 The 24-hourly pattern is able to show persistence effects in relation to the diurnal cycle. Fig. 7
363 shows *MD*, *SDD* and *MROCD* patterns for a day-night period derived from 1440 TIR images.

364 The 24-hourly *MD* median is negative (-25.5 W m^{-2}). In addition, the 80 % percentile is
365 slightly negative (-1.4 W m^{-2}). For all selected AOI (see Fig. 7, left) the spatial average of
366 *MD*, *SDD* and *MROCD* are summarised in Table 2. The sunlit treetop AOI has a slight higher
367 *MD* (-22.9 W m^{-2}) in comparison to the temporarily shadowed treetop AOI (-24.9 W m^{-2}).

368 Even the car-park area between the parked cars and therefore situated in the car shadow has

369 negative *MD* values (AOI 8). The car surfaces (AOI 11) and the car-park area covered by
 370 concrete paving stones (AOI 9 and AOI 12) show positive *MD* values in spite of afternoon
 371 tree shadow. In this thermal pattern, a hot spot corresponds to the eastern part of the car-park
 372 area. The whole car-park shows a slight gradient from the hot eastern to the western part. This
 373 thermal gradient is a persistence effect resulting from the history of shadow.

374 The diurnal *SDD* median (55 W m^{-2}) is higher than the three-hourly median values (Fig. 7,
 375 middle). This results from the accumulation of day and night differences between the
 376 courtyard and the roof. For instance, the asphalt loading zone and the wall show the highest
 377 *SDD* values as a consequence of completely different conditions during the day (shadow) and
 378 during the night (lower SVF) in comparison to the roof. The car surfaces show also high *SDD*
 379 values. This is a consequence of car movement and thermal performance of metallic surfaces.



380
 381 **Figure 7: Spatio-temporal patterns of mean difference (*MD*) (left column), standard deviation of**
 382 **difference (*SDD*) (middle column) and mean rate of change of difference (*MROCD*) (right column)**
 383 **between upward long-wave radiation from the courtyard and upward long-wave radiation from the roof**
 384 **for a 24-hourly cycle. The *MD* pattern shows the position and number of selected areas of interest (AOI)**
 385 **(see also Table 2).**

386

387 The original 24-hourly *MROCD* values at one minute resolution were multiplied by 1440 to
 388 represent changes at the diurnal scale. Therefore, this pattern comprises spatial information
 389 about alteration in upward long-wave radiation between 06:01 and 06:00 next morning. This
 390 pattern is completely different in comparison to the 24-hourly *MD* and *SDD* patterns. It is not
 391 possible to identify features, which correspond to thermal gradients like the car-park area
 392 shown in the 24-hourly *MD* pattern (Fig. 7, left) or to the dichotomy in terms of northern
 393 sunlit and southern shadowed part.

394 **Table 2: Spatio-temporal average of mean difference (*MD*), standard deviation of difference (*SDD*) and**
 395 **mean rate of change of difference (*MROCD*) for selected areas of interests (AOI) for a diurnal cycle (4th**
 396 **May 06:01 to 5th May 06:00 CET), see also figure 7 (left) for AOI positions.**

AOI number	AOI description (AOI pixel size)	<i>MD</i> (Wm ⁻²)	<i>SDD</i> (Wm ⁻²)	<i>MROCD</i> (Wm ⁻² day ⁻¹)
1	Terrace gravel (16 x 13)	-62.0	61.8	-0.7
2	Terrace hedgerow (81 x 13)	-43.9	56.3	+8.1
3	Asphalt loading zone, central (21 x 21)	-41.3	60.6	-5.2
4	Asphalt loading zone, left (21 x 21)	-28.1	62.6	-4.3
5	Treetop, shadowed (66 x 16)	-24.9	53.7	-1.9
6	Treetop, sunlit (66 x 66)	-22.9	46.1	-1.4
7	Wall (26 x 5)	-24.3	61.9	-4.9
8	Honeycomb-type paving stones with grass (6 x 17)	-7.1	34.2	-4.5
9	Concrete paving stones, West (36 x 11)	+5.5	36.0	-3.5
10	Honeycomb-type paving stones with grass (20 x 5)	+21.0	25.5	-4.0
11	Car (10 x 10)	+22.2	52.3	-9.9
12	Concrete paving stones, East (41 x 11)	+28.0	31.4	-2.0

397

398 On closer examination, the 24-hourly *MROCD* pattern shows lower values for the loading

399 zone than for the car-park area. Furthermore, shadow due to parked cars produced the lowest

400 *MROCD* values. Therefore, this pattern can be explained by the history of shadow. In general,

401 we measured a slight decrease of upward long-wave radiation flux density for artificial

402 courtyard surfaces in this 24-hourly period. Only the hedgerow on the terrace has a positive

403 rate of change. The biomass of the vegetation is not able to store or conduct heat into ground

404 in the same way as artificial surfaces. Air temperature is very important for modulation of

405 vegetation surface temperature (Oke, 1987, p. 121) and upward long-wave radiation

406 respectively. The measured air temperatures can be used to explain *MROCD* pattern for the

407 hedgerow. We installed an air temperature sensor (Campbell CS 215) 1.3 m above the terrace

408 and very close to the hedgerow. We measured an increase in air temperature of 1 K for this

409 24-hourly period from 4th May 06:01 to 5th May 06:00. This might be the reason for the

410 positive hedgerow *MROCD* value. At roof level, the air temperature measurements showed no
411 change. Interestingly some branches show higher *MROCD* values than the rest of the treetop.
412 These parts are probably more influenced by turbulence processes.

413

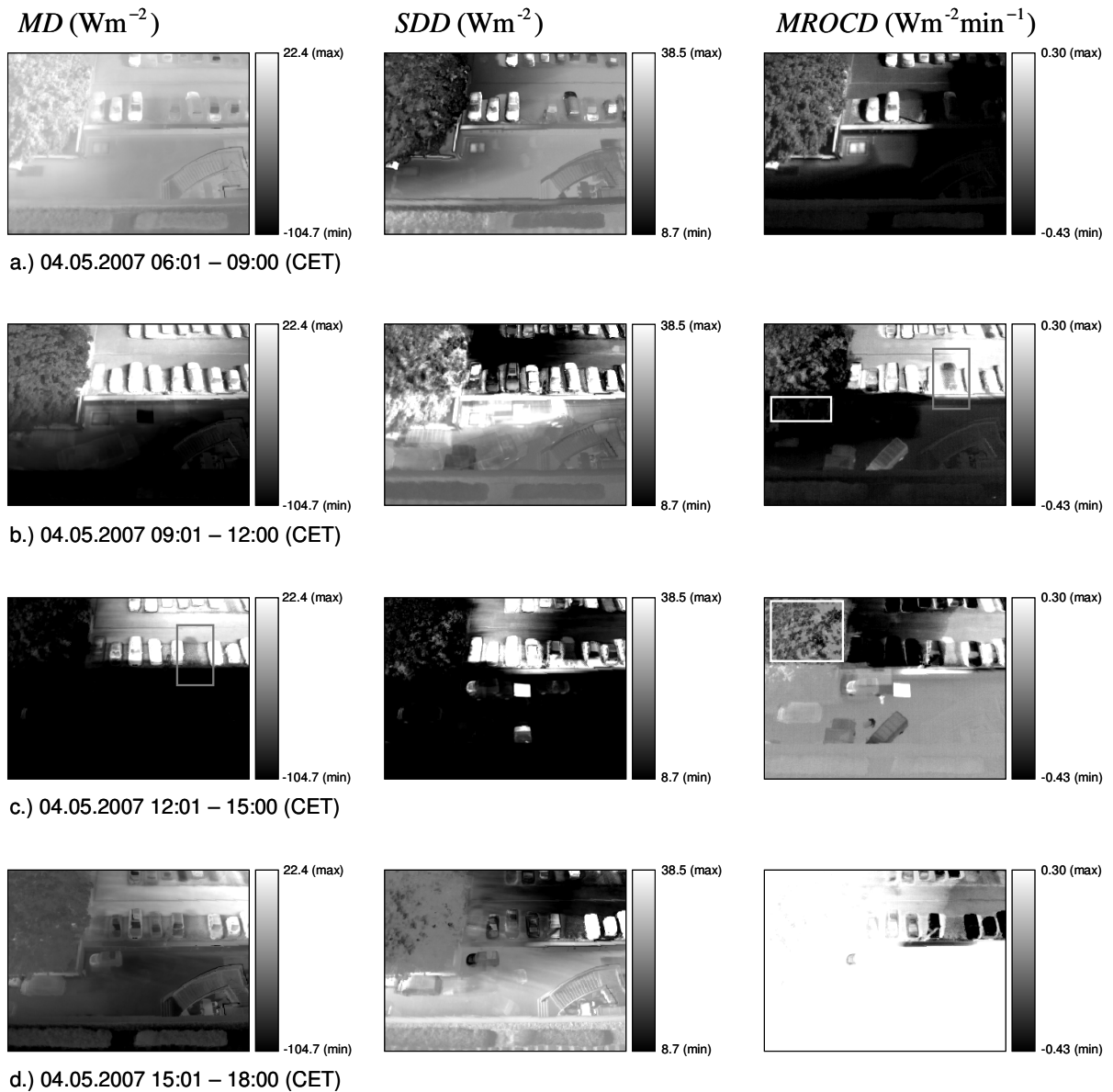
414 4. Discussion

415 This section discusses the temporal variability of $\uparrow\Delta E(\bar{x}_i, t)$ patterns and the temporal
416 variability of $\uparrow\Delta E(\bar{x}_i, t)$ for specific AOI in the courtyard during the TST investigation period.
417 Furthermore, we discuss an approach to determine the surface thermal admittance using the
418 attenuation of the thermal persistence signal.

419

420 4.1 Temporal variability of thermal patterns

421 A grey-scaling visualization approach using fixed minimum and maximum brightness values
422 allows interpretation of temporal changes between the three-hourly thermal patterns. This
423 visualization approach is critical for the night period with overall lower values because of
424 different thermal regimes during day and night. Therefore, we considered day and night
425 separately. For all daytime patterns (Fig. 8), the maximum brightness value represents the
426 average of the 95 % percentiles and the minimum brightness value represents the average of
427 the 5 % percentiles from all four daytime periods i.e. from 06:01 to 18:00 in Fig. 6. The same
428 approach was applied for visualisation of patterns from 18:01 to 06:00 next morning.



429

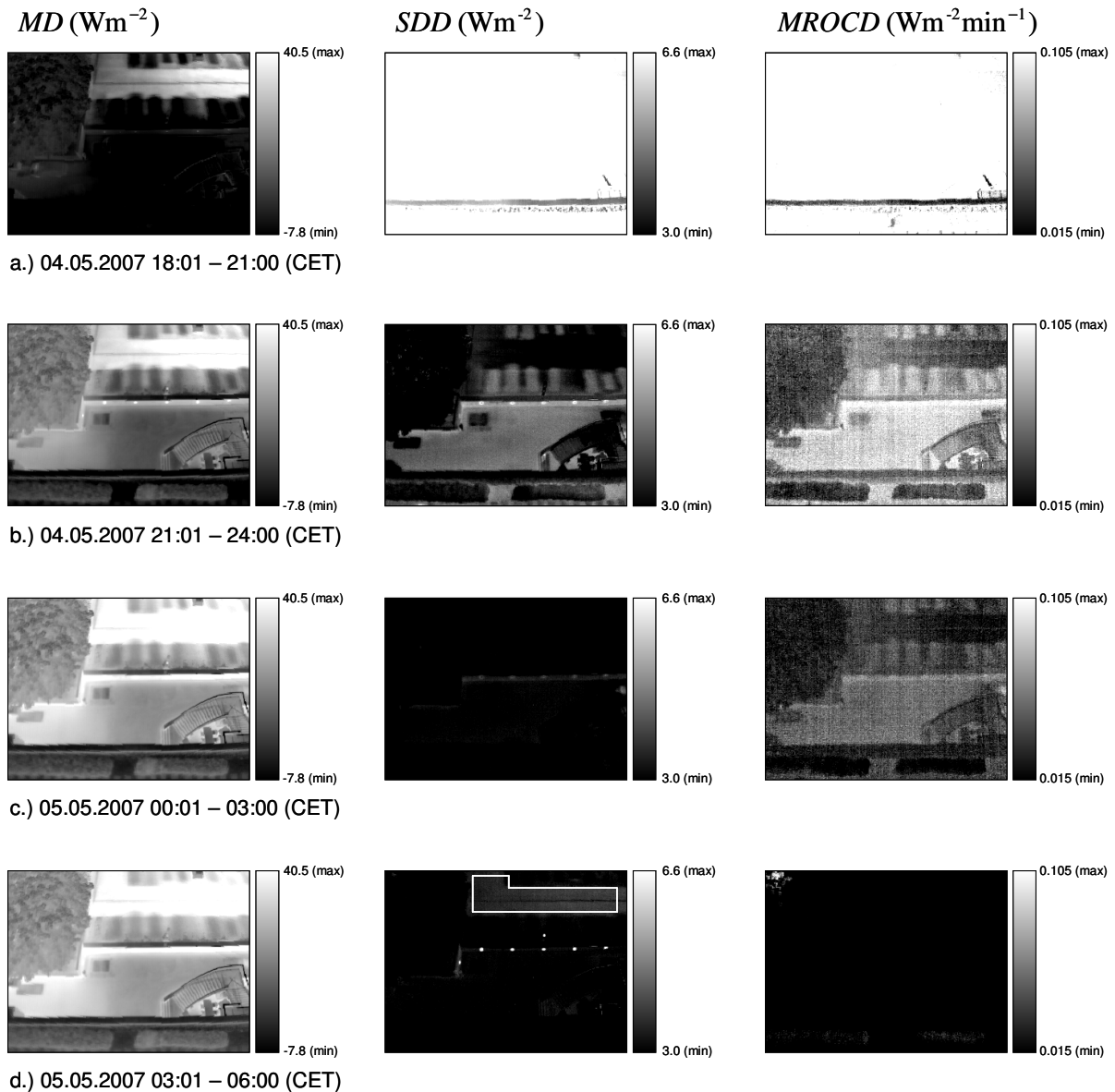
430 **Figure 8: Spatio-temporal patterns of mean difference (*MD*) (left column), standard deviation of**
 431 **difference (*SDD*) (middle column) and mean rate of change of difference (*MROCD*) (right column)**
 432 **between upward long-wave radiation from the courtyard and upward long-wave radiation from the roof.**
 433 **Visualization is based on fixed brightness values derived from the three-hourly daytime median values**
 434 **(06:01 to 18:00 4th May 2007 CET).**

435

436 During the day, thermal hot spots in the *MD* patterns are clearly associated with sunlit car
 437 surfaces, sunlit pavements or car engines. The shadowed half of the courtyard dominates the
 438 daily *MD* patterns. After 09:00 until sunset all treetop pixel have negative *MD* values. With
 439 respect to the treetop, we can separate two phases. In the morning pattern from 09:00 to
 440 12:00, the building shadow caused lower *MROCD* values for the shadowed treetop area than
 441 the supposed transpiration process for the sunlit crown apex (Fig. 8b, right, white box). Later

442 on in the noon pattern from 12:00 to 15:00, the sunlit crown area shows lower *MROCD*
443 values (Fig. 8c, right, white box).

444 Generally, during the night *MD* is positive because of a small SVF for the courtyard surfaces
445 compared the roof. The influence of SVF distribution within the courtyard is remarkable for
446 the loading zone. Between the tree and the Stilwerk building, we can expect lower SVF than
447 for the centre of the loading zone. The *MD* patterns in Fig. 9 (left) show higher values for the
448 area between the tree and the Stilwerk building. This result corresponds to other studies about
449 SVF in urban areas and its influence on surface temperatures (e.g. Eliasson 1992). The small
450 wall shows the highest *MROCD* values (Fig. 9b, right). The restricted sky view results in an
451 increase of *MD* during the night. For the night, the fixed brightness visualisation approach
452 shows a slight equalisation tendency in the thermal patterns. For instance, the cold spots from
453 the formerly shadowed parking spaces (Fig. 9a, left) diminish clearly but are visible at the end
454 of the night (Fig. 9d, left). In general, the *MROCD* pattern provides insight into the spatio-
455 temporal development of the thermal patterns. Strong changes in $\uparrow \Delta E(\bar{x}_i, t)$ are detectable in
456 the consecutive three-hourly *MD* patterns. For instance, an overall strong change (high
457 brightness) dominates the *MROCD* pattern in Fig. 9a (right) whose effects are visible in the
458 consecutive *MD* pattern (Fig. 9b, left) by overall higher values.



459

460 **Figure 9: Spatio-temporal patterns of mean difference (MD) (left column), standard deviation of**
 461 **difference (SDD) (middle column) and mean rate of change of difference ($MROCD$) (right column)**
 462 **between upward long-wave radiation from the courtyard and upward long-wave radiation from the roof.**
 463 **Visualization is based on fixed brightness values derived from the three-hourly nighttime median values**
 464 **(18:01 4th May to 06:00 5th May 2007 CET). The white spots in the SDD pattern (b, c, d) are wall lights.**

465

466 4.2 Temporal variability of selected areas of interest (AOI)

467 Now, we discuss the temporal variability of $\uparrow \Delta E(\bar{x}_i, t)$ for the AOI numbers 2, 5, 6, 9 and 12

468 from Table 2. Considerable differences show the sunlit and the shadowed vegetation AOI in

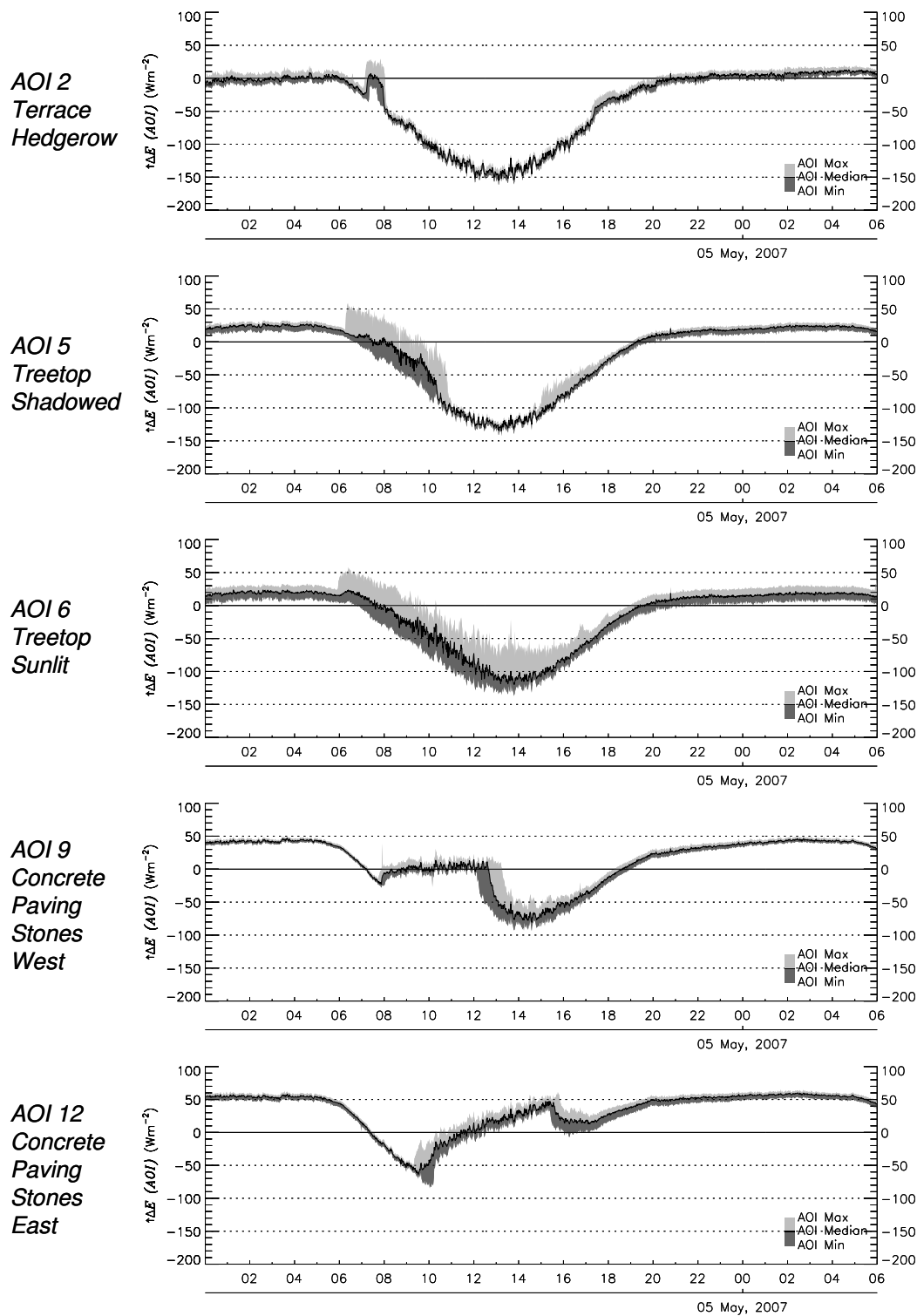
469 Fig. 10. The range between the AOI maximum and AOI minimum data is higher for the sunlit

470 treetop. Here alteration between sunlit and shadowed leaves produces a higher variability than

471 for the almost shadowed hedgerow. Between 11:00 and 15:00, the graph of the shadowed
472 treetop has the same shape like the hedgerow graph. The variability (AOI 2) is higher around
473 08:00 and 18:00 when the hedgerow receives direct solar irradiance. The sunlit treetop data
474 are positively skewed in the noon period between 13:00 and 15:00. This could be a
475 consequence of reduced leaf transpiration due to stomata closure or due to the angle between
476 Sun and leaf orientation resulting in a higher amount of sunlit parts.

477 Interestingly the difference between sealed courtyard surfaces and roof does not increase
478 during the whole night in spite of reduced SVF. Shortly after sunset around 20:00, the
479 differences only slightly increase for all AOI. Between 02:00 and 04:00 (5th May) the
480 differences, even slightly decrease for the concrete paving stones. The explanation for these
481 temporal changes of difference between car-park surface and roof may be as follows. The
482 CNR1 radiation data from the roof shows that net long-wave radiation changes from -280
483 W m^{-2} at 14:00 (30 min average) to -117 W m^{-2} at 20:00 and remains around -70 W m^{-2}
484 between 02:30 and 04:30. Thus, the role of net long-wave radiation in the cooling process of
485 the roof becomes weaker. Additionally, sensible heat flux density measurements above the
486 roof (37.5 metres above street and 10.2 metres above roof) show a downward sensible flux
487 density between 39 W m^{-2} and 8 W m^{-2} after sunset (19:30 to 21:30). This period after
488 sunset where energy is transported to the surface is also mentioned in Christen & Vogt
489 (2004). Later, sensible heat flux density alternated between 9 W m^{-2} (downward) and -13
490 W m^{-2} (upward). Observations of local-scale sensible heat flux density in urban areas show
491 persistence of slight upward sensible heat flux density from the warmer urban canopy layer
492 throughout the night (Oke 1988, Christen & Vogt 2004, Grimmond et al. 2004). A study
493 based on urban energy balance modelling from Harman & Belcher (2006) suggests a
494 mechanism for this effect. They argue that the urban boundary layer air is cooler than the
495 surface temperature in the street canyon, because of greater downward sensible heat flux

496 density from the urban boundary layer to the roof and higher heat capacity for street canyon
497 surfaces and reduced SVF. The result is a slight upward sensible heat flux density from the
498 street canyon into the urban boundary layer throughout the night (Harman & Belcher 2006).
499 Therefore, we suggest also a slight upward sensible heat flux density from the hotter surfaces
500 inside the courtyard throughout the night, which influences the temporal variability of the
501 difference between upward long-wave radiation from sealed courtyard surfaces and the roof.
502 Also in the *SDD* pattern (Fig. 9d, middle, white box) the hotter pavement area and the wall
503 are the only detectable features in the courtyard.
504 These results tend to mimic the difference between the cooling curves typical of urban and
505 rural surfaces, especially where a rural surface is considered dry (e.g. Johnson et al. 1991,
506 Oke et al. 1991). Another process that could influence the differences in upward long-wave
507 radiation is the slumping of cold air from the building roof into the courtyard, which could
508 affect the convective exchange of heat between the sealed courtyard surfaces and the
509 atmosphere.



510

511 **Figure 10: Temporal variability of difference between upward long-wave radiation from areas of interest**
 512 **(AOI) in the courtyard and upward long-wave radiation from the roof.**

513

514 *4.3 Derivation of surface thermal admittance by means of TST*

515 We examined the attenuation of persistence effects for the analysis of thermal patterns and

516 their relation to surface thermal properties. For this purpose, we look at a phenomenon, which

517 is detectable in the noon *MD* pattern (Fig. 8c, left, grey box). One parking space appears with
 518 lower *MD* values by the shape of the formerly parked car. The departure of the car caused a
 519 persistence effect lasting over three hours. Departure from the car-park caused a decrease in
 520 $\hat{E}_{TST}(\bar{x}_i, t)$ which is clearly visible in the *MROCD* pattern (Fig. 8b, right, grey box). This car-
 521 shaped pattern is barely visible in the following *MD* patterns (Fig. 8d, left). Attenuation of the
 522 difference caused by temporary disturbances due to parked cars was further analysed.

523 Difference $\hat{\Delta E}_{ref}(t)$ between temporarily shadowed and non-shadowed surfaces inside the
 524 courtyard is defined as:

$$525 \quad \hat{\Delta E}_{ref}(t) = \left\langle \hat{E}_{TST}(\bar{x}_{shd}, t) \right\rangle - \left\langle \hat{E}_{TST}(\bar{x}_{ref}, t) \right\rangle, \quad (7)$$

526 where $\left\langle \hat{E}_{TST}(\bar{x}_{shd}, t) \right\rangle$ is the spatial mean of the temporarily shadowed parking space and

527 $\left\langle \hat{E}_{TST}(\bar{x}_{ref}, t) \right\rangle$ is the spatial mean of neighbouring non-shadowed reference surface. It is

528 important to note that the considered surfaces are composed of the same material. We found

529 several temporary persistence effects in the TIR imagery dataset. For the description of the

530 decrease of $\hat{\Delta E}_{ref}(t)$ in the course of time, we found the following modified exponential

531 function:

$$532 \quad \hat{\Delta E}_{ref}(t - t_0) = \hat{\Delta E}_{ref}(t_0) \exp\left(-\sqrt{\frac{t - t_0}{\tau}}\right), \quad (8)$$

533 where $\hat{\Delta E}_{ref}(t - t_0)$ is the difference of upward long-wave radiation flux density in the

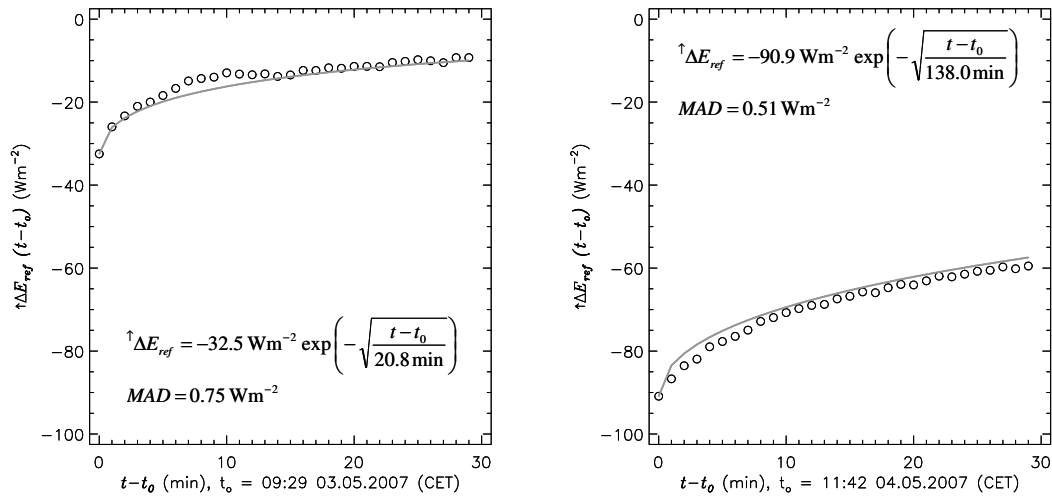
534 course of time after car departure, and $\hat{\Delta E}_{ref}(t_0)$ is the difference of upward long-wave

535 radiation flux density between formerly shadowed and non-shadowed surface immediately

536 after car departure. The time-constant τ is defined as:

$$537 \quad \frac{\hat{\Delta E}_{ref}(\tau)}{\hat{\Delta E}_{ref}(t_0)} = \exp(-1). \quad (9)$$

538 We applied a two parameter fit method to determine τ using Eq. 8 and measured TIR data.
 539 The following graphs in Fig. 11 show good agreement between computed data from Eq. 8
 540 (grey curve) and measured TIR data (black circle) for two cases regarding concrete paving
 541 stone material.



542
 543 **Figure 11: Equalization of the difference between upward long-wave radiation from the temporarily**
 544 **shadowed car-park surface and the reference surface (concrete paving stones) close to it. Decay curves**
 545 **derived from exponential equations noted and based on Eq. 8. Left graph refers to case 1 and right graph**
 546 **refers to case 2. The MROCD pattern in Fig. 8b (right) corresponds to case 2. MAD is the mean absolute**
 547 **deviation between measured TIR data (Eq. 7) and the data using the computed time constant τ from Eq.**
 548 **8.**

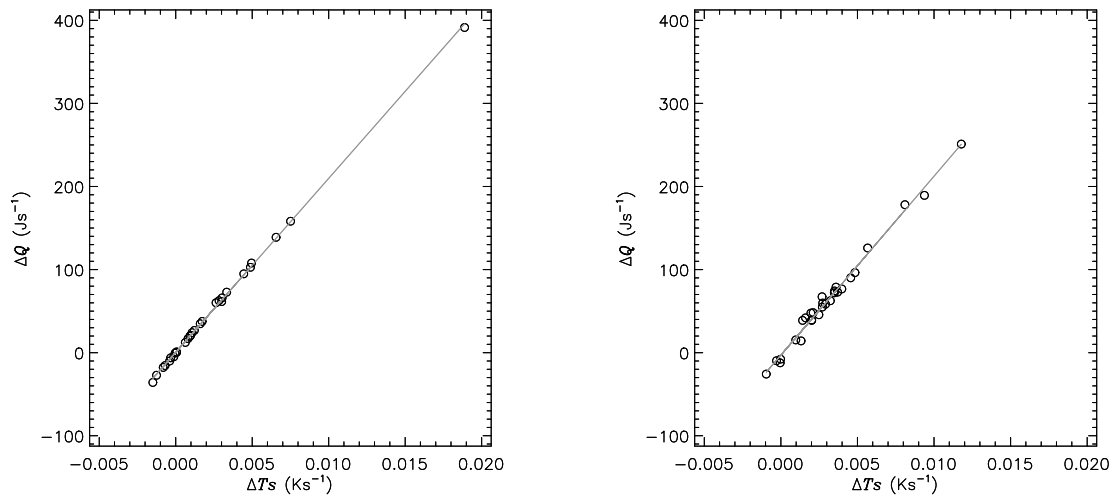
549
 550 If we compare the radiation balance of the two surfaces after car departure, then they differ
 551 only in respect to upward long-wave radiation. Therefore, we consider $\hat{\Delta E}_{ref}(t-t_0)$ as the
 552 relevant heat flux responsible for the attenuation of the persistence effect. In other words, the
 553 temporarily disturbed surface should have a higher rate of change (ROC) of surface
 554 temperature (T_s) than the reference surface close to it due to lower upward long-wave
 555 radiation. The approach summarizes the influence of further heat fluxes contributing to
 556 surface warming of the formerly shadowed surface in ΔQ_{res} , which is approximated to be
 557 constant. An appropriate thermal property governing the heating or cooling rate of a surface
 558 to a given heat flux is the thermal admittance (μ), defined by the thermal conductivity (k) and
 559 volumetric heat capacity (C) of the surface:

560
$$\mu = \sqrt{kC} . \quad (10)$$

561 The following equation (based on Zmarsly et al. 2002, p. 57) is used for the determination of
 562 μ :

563
$$\Delta Q = \frac{2A\sqrt{\Delta t}}{\sqrt{\pi}} \cdot \mu \cdot \Delta T_s + \Delta Q_{res} = c \cdot \mu \cdot \Delta T_s + \Delta Q_{res} , \quad (11)$$

564 where ΔQ is defined as the ROC of $\uparrow \Delta E_{ref}(t - t_0)$, multiplied by Δt , the constant
 565 measurement interval of 60 s. A is the active surface area set to unity (1 m^2). ΔT_s is defined
 566 as the ROC of the difference between T_s of the formerly shadowed surface and the reference
 567 surface. T_s is derived from the original TIR data using an emissivity value of 0.95. The
 568 following graphs in Fig. 12 show scatter plots of ΔT_s vs. ΔQ for two cases.



569
 570 **Figure 12: Scatter plots of ΔT_s vs. ΔQ derived from TST data presented in Fig. 11. Table 3 summarizes**
 571 **all regression parameters of the two analysed persistence effects. Left graph refers to case 1 and right**
 572 **graph refers to case 2.**

573
 574 Finally, μ is obtained from a linear regression fit using Eq. 11 and the data of the first 30
 575 minutes of the persistence attenuation process. Table 3 summarizes the two analysed
 576 persistence effects. The derived thermal admittance values for dense concrete surfaces are in
 577 the range of literature values e.g. $1785 \text{ J m}^{-2} \text{ s}^{-0.5} \text{ K}^{-1}$ (Oke 1987), $2349 \text{ J m}^{-2} \text{ s}^{-0.5} \text{ K}^{-1}$ (Stull

578 1988) or $3180 \text{ J m}^{-2} \text{ s}^{-0.5} \text{ K}^{-1}$ (Zmarsly et al. 2002). In both cases ΔQ_{res} is very low. The
 579 higher value in case 2 could be attributed to a higher influence of sensible heat exchange at
 580 noon time.

581 **Table 3: Fit parameters and thermal admittance of concrete paving stone material derived from the**
 582 **attenuation of thermal persistence effects caused by parked cars in the courtyard.**

Case	Duration of disturbance (min)	R^2	$\mu_{concrete}$ ($\text{J m}^{-2} \text{ s}^{-0.5} \text{ K}^{-1}$)	ΔQ_{res} (J s^{-1})
1	22	0.999	2395	0.35
2	269	0.989	2464	-3.03

583

584 6. Conclusion

585 The TIR ground-based remote sensing approach applied here is highly suitable to investigate
 586 dynamic processes within complex 3D urban structures. In addition, TST holds the possibility
 587 to assess the accuracy of 3D simulators, which produce high-resolution TIR or surface
 588 temperature scenes (Poglio et al. 2006). Further experimental studies of spatio-temporal
 589 thermal patterns need a method for handling surface emissivity at these scales. The effect of
 590 differences in atmospheric path lengths could be important for studying an extended FOV e.g.
 591 complete urban quarters by using a skyscraper as TIR camera platform.

592 Our findings indicate the influence of shadow on spatio-temporal patterns of upward long-
 593 wave radiation flux density from an urban courtyard. We can conclude that the history of
 594 shadow i.e. when shadow is present on the surface is important for the 24-hourly *MD* pattern.

595 The thermal hot spot corresponds to the pavement area, which was non-shadowed between
 596 10:00 and 15:30. The thermal cold spot corresponds to the shadowed part of the courtyard.

597 The lime tree appears also as a cold spot due to transpiration. The 24-hourly *MROCD* pattern
 598 depends on shadow duration i.e. how long shadow has been present on the surface and on air

599 temperature changes. The three-hourly patterns show persistence effects because of shadow,

600 SVF distribution, surface material, human activities and turbulence characteristics of the

601 surface-atmosphere interface. In order to prove the assumed SVF distribution in the courtyard
602 and to make spatial correlations with thermal patterns it is possible to apply urban digital
603 elevation models in raster format (e.g. Lindberg 2007) or models using vector data (e.g. Teller
604 & Azar 2001).

605 Our results reveal a basic phenomenon in relation to the interpretation of nocturnal TIR
606 images, because thermal persistence effects could continue to the night. Surfaces where
607 shadow is present in the afternoon potentially show persistence of thermal patterns far into the
608 night or in the case of parked cars to the next morning. With a reasonable certainty, we expect
609 a ‘nighttime bias’ for these surfaces, which has to be considered e.g. in study of relations
610 between urban morphology and nighttime thermal patterns.

611 The analysis of attenuation of upward long-wave radiation difference between temporarily
612 shadowed and non-shadowed concrete surfaces inside the courtyard provides an opportunity
613 to derive the surface thermal admittance. In order to verify this method it is necessary to carry
614 out a controlled experiment. Further studies will address derivation of surface thermal
615 properties from TST as well as the role of sensible heat exchange during the equalization of
616 persistence effects.

617

618 7. Acknowledgements

619 We are especially grateful to Andreas Christen (Department of Geography and Atmospheric
620 Science Program, University of British Columbia), who provided the procedure for
621 radiometric correction of lens effects and made valuable comments on the manuscript.
622 Furthermore, gratefully acknowledge to our colleges at the Chair of Climatology. Special
623 thanks go to H. Küster, M. Otto, and J. Rogée who helped substantially in the design of the
624 experiment and for helping to set up and maintain the meteorological measurement sites. The

625 authors would like to thank R. Finkelburg, F. Maussion and the reviewers for their
626 comments, which helped to improve the quality of this paper.

627

628 8. References

629 Bruse, M. & Fleer, H. (1998). Simulating surface-plant-air interactions inside urban
630 environments with a three dimensional numerical model. *Environmental Modelling &*
631 *Software*, 13, 373-384.

632

633 Christen, A. & Vogt, R. (2004). Energy and radiation balance of a central European city.
634 *International Journal of Climatology*, 24, 1395-1421.

635

636 Christen, A., Scherer, D. & Mielke, M. (2006). High frequency patterns in urban surface
637 temperatures. *European Association of Remote Sensing Laboratories (EARSeL) – First*
638 *Workshop of the Special Interest Group on Urban Remote Sensing, March 2-3 2006, Berlin,*
639 *Germany.*

640

641 Chudnovsky, A., Ben-Dor, E. & Saaroni, H. (2004). Diurnal thermal behavior of selected
642 urban objects using remote sensing measurements. *Energy and Buildings*, 36, 1063-1074.

643

644 Eliasson, I. (1992). Infrared thermography and urban temperature patterns. *International*
645 *Journal of Remote Sensing*, 13, 869-879.

646

647 Endlicher, W. & Lanfer, N. (2003). Meso- and micro-climatic aspects of Berlin's urban
648 climate. *Die Erde*, 134, 277-293.

649

650 Erell, E. & Williamson, T. (2007). Intra-urban differences in canopy layer air temperature at a
651 mid-latitude city. *International Journal of Climatology* 27, 1243-1255.
652

653 Grimmond, C. S. B., Salmond, J. A., Oke, T. R., Offerle, B. & Lemonsu, A. (2004). Flux and
654 turbulence measurements at a densely built-up site in Marseille: Heat, mass (water and carbon
655 dioxide), and momentum. *Journal of Geophysical Research Atmospheres*, 109, D24101,
656 doi:10.1029/2004JD004936.
657

658 Harman, I. N. & Belcher, S. E. (2006). The surface energy balance and boundary layer over
659 urban street canyons. *The Quarterly Journal of the Royal Meteorological Society*, 132, 2749-
660 2768.
661

662 Hoyano, A., Asano, K. & Kanamaru, T. (1999). Analysis of the sensible heat flux from the
663 exterior surface of buildings using time sequential thermography. *Atmospheric Environment*,
664 33, 3941-3951.
665

666 Johnson, G., Oke, T. R., Lyons, T., Steyn, D., Watson, I. & Voogt, J. (1991). Simulation of
667 surface urban heat islands under 'IDEAL' conditions at night part 1: Theory and tests against
668 field data. *Boundary-Layer Meteorology* 56, 275-294.
669

670 Kobayashi, T. & Takamura, T. (1994). Upward longwave radiation from a non-black urban
671 canopy. *Boundary-Layer Meteorology*, 69, 201-213.
672

673 Kottmeier, C., Biegert, C. & Corsmeier, U. (2007). Effects of urban land use on surface
674 temperature in Berlin: Case study. *Journal of Urban Planning and Development*, 133, 128-
675 137.

676

677 Lagouarde, J. P., Ballans, H., Moreau, P., Guyon, D. & Coraboeuf, D. (2000). Experimental
678 study of brightness surface temperature angular variations of maritime pine (*Pinus pinaster*)
679 stands. *Remote Sensing of Environment*, 72, 17-34.

680

681 Lagouarde, J. P., Moreau, P., Irvine, M., Bonnefond, J. M., Voogt, J. A. & Sollic, F. (2004).
682 Airborne experimental measurements of the angular variations in surface temperature over
683 urban areas: case study of Marseille (France). *Remote Sensing of Environment*, 93, 443-462.

684

685 Lindberg, F. (2007). Modelling the urban climate using a local governmental geo-database.
686 *Meteorological Applications*, 14, 263-273

687

688 Lo, C. P., Quattrochi, D. A. & Luvall, J. C. (1997). Application of high-resolution thermal
689 infrared remote sensing and GIS to assess the urban heat island effect. *International Journal*
690 *of Remote Sensing*, 18, 287-304.

691

692 Mertens, E. (1999). Bioclimate and city planning – open space planning. *Atmospheric*
693 *Environment*, 33, 4115-4123.

694

695 Munier, K. & Burger, H. (2001). Analysis of land use data and surface temperatures derived
696 from satellite data for the city of Berlin. In C. Jürgens (Ed.), *Remote Sensing of Urban*

697 *Areas/Fernerkundung in urbanen Räumen. Heft 35*, (pp. 206-221). Regensburg:
698 Regensburger Geographische Schriften.
699
700 Nichol, J. (2005). Remote sensing of urban heat islands by day and night. *Photogrammetric*
701 *Engineering & Remote Sensing*, 71, 613-621.
702
703 Oke, T. R. (1987). *Boundary Layer Climates*. Methuen, New York, 435 pp.
704
705 Oke, T. R. (1988). The urban energy balance. *Progress in Physical Geography*, 12, 471-508.
706
707 Oke, T. R., Johnson, G., Steyn, D. & Watson, I. (1991). Simulation of surface urban heat
708 islands under 'ideal' conditions at night part 2: Diagnosis of causation. *Boundary-Layer*
709 *Meteorology* 56, 339-358.
710
711 Quattrochi, D. A. & Ridd, M. K. (1994). Measurements and analysis of thermal energy
712 responses from discrete urban surfaces using remote sensing data. *International Journal of*
713 *Remote Sensing*, 15, 1991-2022.
714
715 Poglio, T., Mathieu-Marni, S., Ranchin, T., Savania, E. & Wald, L. (2006). OSrIS: a
716 physically based simulation tool to improve training in thermal infrared remote sensing over
717 urban areas at high spatial resolution. *Remote Sensing of Environment*, 104, 238-246.
718
719 Rigo, G., Parlow, E. & Oesch, D. (2006). Validation of satellite observed thermal emission
720 with in-situ measurements over an urban surface. *Remote Sensing of Environment*, 104, 201-
721 210.

722

723 Ruffieux, D., Wolfe, D. E. & Russel, C. (1990). The effect of building shadows on the
724 vertical temperature structure of the lower atmosphere in downtown Denver. *Journal of*
725 *Applied Meteorology*, 29, 1221-1231.

726

727 Spronken-Smith, R. A. & Oke T. R. (1999). Scale modelling of nocturnal cooling in urban
728 parks. *Boundary-Layer Meteorology*, 93, 287-312.

729

730 Stull, R.B. (1988). An introduction to boundary layer meteorology. Kluwer Academic
731 Publishers, 666 pp.

732

733 Sugawara, H., Narita, K. & Mikami, T. (2001). Estimation of effective thermal property
734 parameter on a heterogeneous urban surface. *Journal of the Meteorological Society of Japan*,
735 79, 1169-1181.

736

737 Sugawara, H. & Takamura, T. (2006). Longwave radiation flux from an urban canopy:
738 Evaluation via measurements of directional radiometric temperature. *Remote Sensing of*
739 *Environment*, 104, 226-237.

740

741 Teller, J. & Azar, S. (2001). Townscope II – A computer systems to support solar access
742 decision-making. *Solar Energy*, 70, 187-200.

743

744 Voogt, J. (2008). Assessment of an Urban Sensor View Model for thermal anisotropy. *Remote*
745 *Sensing of Environment*, 112, 482-495.

746

- 747 Voogt, J. A. & Oke, T. R. (1998). Effects of urban surface geometry on remotely-sensed
748 surface temperature. *International Journal of Remote Sensing*, 19, 895-920.
749
- 750 Voogt, J. A. & Oke, T. R. (2003). Thermal remote sensing of urban climates. *Remote Sensing*
751 *of Environment*, 86, 370-384.
752
- 753 Zmarsly, E., Kuttler, W. & Pethe, H. (2002). Meteorologisch-klimatologisches Grundwissen.
754 Ulmer, Stuttgart, 176 pp. (in German).